Chemical Engineering Journal 462 (2023) 142007

Contents lists available at ScienceDirect

Chemical Engineering Journal

journal homepage: www.elsevier.com/locate/cej

Self-seeded coprecipitation flow synthesis of iron oxide nanoparticles via triphasic reactor platform: Optimising heating performance under alternating magnetic fields

Sayan Pal [a], Maximilian O. Besenhard [a], Liudmyla Storozhuk [b], Martin R. Lees [c], Nguyen Thi Kim Thanh [b,d], Asterios Gavriilidis [a,*]

[a] Department of Chemical Engineering, University College London, Torrington Place, London WC1E 7JE, United Kingdom
[b] Biophysics Group, Department of Physics and Astronomy, University College London, Gower Street, London WC1E 6BT, United Kingdom
[c] Department of Physics, University of Warwick, Coventry CV47AL, United Kingdom
[d] UCL Healthcare Biomagnetics and Nanomaterials Laboratory, University College London, 21 Albemarle Street, London W1S 4BS, United Kingdom

ARTICLE INFO

Keywords:
Fouling-free reactor
Three-phase flow
Iron oxide nanoparticles
Seeded growth co-precipitation
Magnetic hyperthermia
Design of experiments

ABSTRACT

Liquid-liquid segmentation is a common method to prevent reactor fouling when synthesising nanoparticles in flow, despite limiting synthetic protocols to single reagent addition steps before segmentation. This work demonstrates how a modular triphasic (gas–liquid–liquid) flow reactor platform overcomes this limitation, facilitating a continuous and fouling-free four-step co-precipitation flow synthesis of iron oxide nanoparticles (IONPs) for magnetically induced hyperthermia cancer treatment (MHCT). For this and other biomedical applications water-based IONP syntheses such as co-precipitation are favoured, but producing IONPs > 10 nm as needed for MHCT remains challenging. To overcome this size barrier for co-precipitation syntheses, a seeded growth co-precipitation strategy was employed here for the first time. After demonstrating the synthesis in batch, a triphasic flow reactor was developed to translate the multistep batch protocol into flow. Nitrogen gas was used to space the liquid–liquid segmented slugs evenly, enabling self-synchronised solution addition into the aqueous slugs dispersed in heptane. Three additions of the iron precursor solution followed by citric acid solution addition formed the seeds, grew them to larger IONPs and stabilised them. The flow platform was used for screening of the synthetic parameters to optimise the IONP heating performance in an alternating magnetic field, hence investigating their potential as MHCT heating agents. The optimal reactor settings identified made it possible to continuously synthesise 0.46 g_{IONPs}/h colloidally stable IONPs in the aqueous phase of size ~15 nm. The fouling-free flow reactor operated at short overall residence times (<5 min) using just ferric and ferrous salts, sodium carbonate and citric acid. The IONPs exhibited high heating performance, with an intrinsic loss power up to 3.76 nH m^2 kg_{Fe}^{-1}.

1. Introduction

In the last decade, micro and millifluidic reactors have demonstrated tremendous potential in a wide range of nanomaterial synthesis in a reproducible and high throughput manner [1]. Their advantages include superior heat and mass transport due to the high specific interfacial area allowing for increased control over reaction conditions, accurate control of mixing, residence time and temperature, often resulting in decreased reaction times, higher yields, and better control of nanoparticle size distributions compared to batch systems [2]. Reactor fouling, however, remains a challenge as it can affect the quality of the nanoparticles [3] and, in the worst case, clog the reactor [4,5]. Therefore, non-fouling flow reactors are in demand for fouling prone synthesis, such as for nanoparticles, but also crystallisation [6] and organic chemical reactions [4].

Different strategies have been developed to prevent or reduce fouling and clogging in nanomaterial flow syntheses, which can be primarily classified into three categories; 1) single-phase flow methods, 2) multiphase segmented flow methods, and 3) alternate reactor designs that mitigate fouling [4,7]. Single-phase flow methods involve

* Corresponding author.
E-mail address: a.gavriilidis@ucl.ac.uk (A. Gavriilidis).

https://doi.org/10.1016/j.cej.2023.142007
Received 16 October 2022; Received in revised form 22 January 2023; Accepted 16 February 2023
Available online 20 February 2023

ultrasound irradiation to prevent clogging [8], increasing electrostatic repulsion between particles and reactor wall by using high negative (or positive) zeta potentials of wall surface in alkaline solutions [9,10]. Such single-phase methods, however, are limited to specific pH regimes and the implementation using micro/ millifluidic systems is often subject to diffusion-limited mixing and reagent dispersion which likely yields broader particle size distributions. In addition, single-phase flow methods cannot prevent fouling during the critical nucleation stage and are not suitable for fast reactions and rapid particle formation. In multiphase methods using immiscible liquid phases, particle–wall interactions are prevented via a layer or thin film of inert carrier phase between the wall and the dispersed reactive phase [11,12]. In addition to improved mixing and mass transfer benefits of micro and millifluidic reactors, liquid–liquid segmented flow provides some unique aspects in particle synthesis. The dispersed liquid phases are isolated by the continuous phase; they can be considered as individual reactors of size comparable to the characteristic reactor length-scale. This feature of liquid–liquid segmentation avoids the unwanted axial dispersion and provides narrow residence time distribution resulting in more monodisperse micro/nanoparticles [13]. Alternatively, continuous reactor designs such as miniature continuous stirred tank reactors (CSTR) in a cascade [14] and open impinging jet reactors [15,16] are reported to have reduced fouling problems for nanoparticle synthesis. This is due to their less confined nature compared to typical micro/ millifluidic reactors, as most nanoparticles are formed distant from the reactor walls, limiting particle wall interactions. CSTR cascades, however, are considered as an intermediate solution between flow and classic batch processes, with mass and heat transfer characteristics closer to batch reactors. Hence, the advantages of micro/millifluidics based flow chemistry do not apply fully in CSTR in series. In contrast, impinging jet reactors offer excellent mixing of reagents and are an ideal solution for rapid, single-step particle forming processes. However, their usage is restricted when multistep reagent addition and long residence times are required. Despite significant developments in scale-up by numbering up and online process screening in flow chemistry, processes involving particle formation still pose significant difficulties. While strides have been made in solving the fouling and clogging issues for nanomaterial synthesis in micro and millifluidic reactors, there is a necessity for further investigation and scope for further improvement.

Among the wide range of magnetic nanoparticles, the synthesis of iron oxide nanoparticles (IONPs) has been well studied and has a diverse range of applications [17,18]. Being biocompatible, magnetic IONPs have been increasingly used over the last decade in biomedical applications such as magnetic resonance imaging, targeted drug delivery, and magnetically induced hyperthermia for cancer treatment (MHCT) with several FDA-approved products [19,20]. MHCT uses the capability of IONPs to emit heat when exposed to an alternating magnetic field [21,22]. Theoretical models [23,24] and experimental studies [25–27] show that monodisperse IONPs >10 nm are better suited for MHCT. Moreover, the clustering of nanoparticles has also been reported to increase MHCT performance in comparison to their core building structures [28,29]. Given the marked dependency of heating performance on particle size [24,30], it appears crucial to increase precisely the size of IONPs for efficient performance in MHCT. The majority of the available literature IONP synthesis protocols which result in high heating rates are usually based on thermal decomposition synthesis [25,28,31], whereas water-based methods struggle to deliver high heating performance [30]. However, thermal decomposition methods involve expensive and toxic organic solvents, require high temperatures (>250 °C), long reaction times, and a time-consuming ligand exchange step for phase transfer, all of which are undesirable. In comparison, water-based synthetic methods such as co-precipitation [32] or partial oxidation [33,34] are considered as simple and economical [35] ways to synthesise IONPs without using harsh reaction conditions and toxic organic solvents. IONPs synthesised by aqueous synthesis methods do not require ligand exchange step for phase transfer, which makes them directly suitable for biomedical applications. IONPs synthesised by co-precipitation in the presence of tiopronin carboxylic acid [36] and using microwave irradiation [29] have shown good magnetic heating performance (intrinsic loss powers of 6.1 and 4.1 nH m^2 kg_{Fe}^{-1}). However, magnetite IONPs bigger than 10 nm suffer from limited shape and particle size control and are not easily accessible using aqueous co-precipitation. Despite the large number of publications using coprecipitation based chemistry, smaller sized particles are mainly reported which have shown poor MHCT performance [30,37,38].

In this work, a seeded growth co-precipitation process is employed to increase the size of IONPs and improve their heating performance. This was possible by utilising the understanding of the particle formation mechanism and kinetics of co-precipitation gained in our previous work [39]. In the seeded growth process, nanoparticle seeds synthesised in the first step are then mixed with a solution composed of metal precursors and capping agents to commence the growth of the seeds. When a significant size increase of the nanoparticles is required, a seeded growth process can be spread out into multiple steps [40]. Though seeded growth strategies have been previously reported for thermal decomposition chemistries to synthesise IONPs [23,28,41,42], their use in co-precipitation chemistries has not been reported, mainly due to the limited information on the particle formation kinetics. The use of a seeded growth strategy for IONP co-precipitation protocols is first reported in the current work, yielding particles with excellent heating performance for hyperthermia applications.

Despite the many examples of liquid–liquid segmenting flow systems in nanomaterial synthesis, its major limitation is multipoint reagent addition [43] for multistep chemistries, such as seeded growth. In addition, liquid–liquid segmenting flow systems usually involve either premixing of reagents in single-phase flow before segmentation with inert carrier phase or reagent mixing during segmentation. This can make the nanoparticles formed susceptible to wall interaction and can cause fouling in chemistries involving fast particle formation kinetics. Duraiswamy and Khan [44] addressed this issue using a very dilute seed formation step in single-phase flow followed by seeded growth in liquid–liquid segmented flow. However, the system was limited to dilute seed concentration and only one step of seeded growth. Nightingale et al. [43] first proposed three-phase flow (liquid–liquid-gas) at μl/min flow rates to enable new reagent addition to the dispersed reacting phase segments without forming new droplets. This strategy of inert gas phase insertion to prevent new reagent droplet formation and to form uniformly spaced three-phase flow has been further used by Wong et al. [45] and Abdel-Latif et al. [46] for Pd nanoparticle and quantum dot synthesis at room temperature conditions, respectively. Karan and Khan et al. [47] used a scaled-up version of the triphasic flow reactor system for nanoparticle catalysed hydrogenation.

A versatile and modular triphasic flow droplet injection reactor system was developed in our recent work, making it possible to robustly add reagents into dispersed phase reacting droplets using temperature controlled capillary based systems [48]. The current work extends this novel triphasic flow reactor to four reagent addition steps into droplets, allowing the reactor platform to be used for three-step seeded growth synthesis of IONPs at elevated temperatures (90 °C) followed by a colloidal stabilisation step, without any fouling and clogging issues. An optimisation study guided by design of experiments (DoE) was performed to find optimum synthesis conditions for IONPs with a high ILP (intrinsic loss power). The simple, cost-effective and environmentally friendly aqueous co-precipitation based synthetic protocol is shown to yield IONPs with excellent heating performance in alternating magnetic fields.

2. Experimental

2.1. Chemicals and materials

Iron (III) chloride hexahydrate (99%), iron (II) chloride tetrahydrate

(99%), sodium carbonate decahydrate (99%) and citric acid (99%) were used as received without any further purification. All solutions were prepared freshly before each experiment using deionised water (15 MΩ). The 0.1 M Fe precursor solution was prepared by mixing 1.802 g iron (III) chloride hexahydrate and 0.6627 g of iron (II) chloride tetrahydrate in 100 ml of deionised water. Hence, the molar $[Fe^{3+}]/[Fe^{2+}]$ ratio was 2:1, which has been shown to give higher purity magnetite (Fe_3O_4) particles [49]. 0.33 M sodium carbonate base solution was used for the coprecipitation, and 0.31 M citric acid solution was used for colloidal stabilisation of the IONPs. All reaction solutions were de-oxygenated via N_2 purging for $>$ 30 min before the experiments. Heptane was used as inert continuous phase for three-phase flow experiments.

2.2. Nanoparticle characterisation

The core diameter (D_{TEM}) of the synthesised IONPs was determined from transmission electron microscope (TEM) images captured at 120 kV acceleration voltage (JEOL 1200 EX). Particle size distributions were obtained by randomly selecting $\geq$ 150 individual particles on different TEM images and measuring their size using ImageJ 1.8. To prepare TEM grids, the IONPs were first precipitated from their solution by adding isopropyl alcohol and then separated by magnetic decantation followed by re-dispersion in DI water via ultra-sonication. Drops of this washed sample solution were then placed on a carbon coated copper grid (200 μm lattice). Different separation methods for IONPs, such as centrifugation and freeze drying, were also investigated and are reported in section 11 in supplementary information. The hydrodynamic diameter, D_h, of the IONPs was measured using dynamic light scattering (DLS) (DelsaMax Pro, Beckman Coulter). X-ray diffraction (XRD) patterns of washed and dried IONP samples were acquired with an X-ray diffractometer (PanAlytical X'Pert Pro, Malvern Instruments) using $Co_{K\alpha}$ (λ = 1.79 Å) radiation source operated at 40 mA and 40 kV. The average crystallite diameter was determined via Scherrer's equation ($D_{XRD} = 0.89\lambda/(B\cos(\theta))$, where D_{XRD} corresponds to average crystallite diameter of a particle, λ is the X-ray wavelength, B is line broadening at half the maximum intensity of the peak, and θ is the diffraction peak angle (2θ = 72° in this work). Precise differentiation between magnetite and maghemite phases is not possible based on XRD pattern(s) [28], and in the current work, references to magnetite are considered as references to magnetite/maghemite mixtures. The nanoparticles' heating abilities in an alternating magnetic field were characterised with a G2 driver D5 series calorimetric analyser from nB nanoScale Biomagnetics at a magnetic field strength of 308 Gauss and a frequency of 488 kHz. The IONPs' ILP, used to compare heating rates measured at different magnetic field strengths and frequencies [50], were determined as described previously [51]. Magnetisation hysteresis curves were determined via a SQUID magnetometer (MPMS, Quantum Design) at 5 K and 300 K. Washed IONP solutions were dried and loaded in a capsule adapted for SQUID measurements. The concentration of Fe in the form of particles was measured via microwave plasma atomic emission spectroscopy (MP-AES, Agilent 4210) as described in [52]. The experimentally measured concentration of Fe was used to calculate the ILP values.

2.3. Design of experiments

Statistical analysis was performed using the JMP Pro software (v.15, SAS Institute Inc.) using the analysis of variance (ANOVA) method at 95% confidence level and least square fit. A custom design analysis was performed to assess the effect of two parameters and the interactions between the two-parameter experiments on the two target responses. DoE comprised of two parameters - the residence time for the seed synthesis and the two growth steps, and the precursor flow rate which was kept the same in each precursor addition step. The residence time for the stabilisation step was not varied and was kept at 1 min. The responses of the DoE matrix were selected as the D_h and the ILP. For verification of the DoE model, six validation experiments were performed at parameter values which were not used by the model during the training steps.

2.4. Self-seeded growth batch co-precipitation synthesis

Batch experiments were performed at 60–90 °C in magnetically stirred 50 ml glass round bottom flasks submerged in a stirred water bath, with nitrogen purge controlled by a mass flow controller (EL-FLOW Prestige, Bronkhorst), and heat and magnetic stirring provided by a hotplate (C-MAG HS10, IKA). A temperature probe (ETS-D5, IKA) measuring the temperature of the stirred water bath was connected to the hotplate for feedback control. 6 ml of Na_2CO_3 base solution was added first into the round bottom flask. Then 6 ml of iron precursor solution was added in three steps; 2 ml at once with 1 min reaction time between the other two additions via a pipette under constant stirring (750 rpm). 1 min after the 3rd addition of the iron precursor, 2.52 ml of citric acid solution (stabiliser) was added to the formed IONP solution (12 ml), which was kept stirring at reaction temperature for another 12 min. A schematic of the seeded growth batch synthesis at 90 °C is shown in Fig. 1.

2.5. Manufacturing and assembly of triphasic reactor platform

Following our recent work [48] a custom-designed fluorinated ethylene propylene (FEP) three-phase droplet generator and four FEP T-junction droplet injectors were used to facilitate IONP seed generation, followed by two feed addition steps to grow these seeds, with intermediate heating between each addition to 90 °C, and a final stabilisation step (see Fig. 2). The FEP reactor components along with hydrophobic FEP tubing (ID = 1 mm, OD = 1/16″, VICI) connecting the reactor elements were used to form a triphasic segmented flow, preventing contact of the reacting aqueous phase with the tubing walls. All inlet and outlet ports of the custom-designed reactor components had ¼-28 flat bottom port configuration to match standard commercially available fluidic connectors. Standard PEEK connectors (IDEX Health Science)

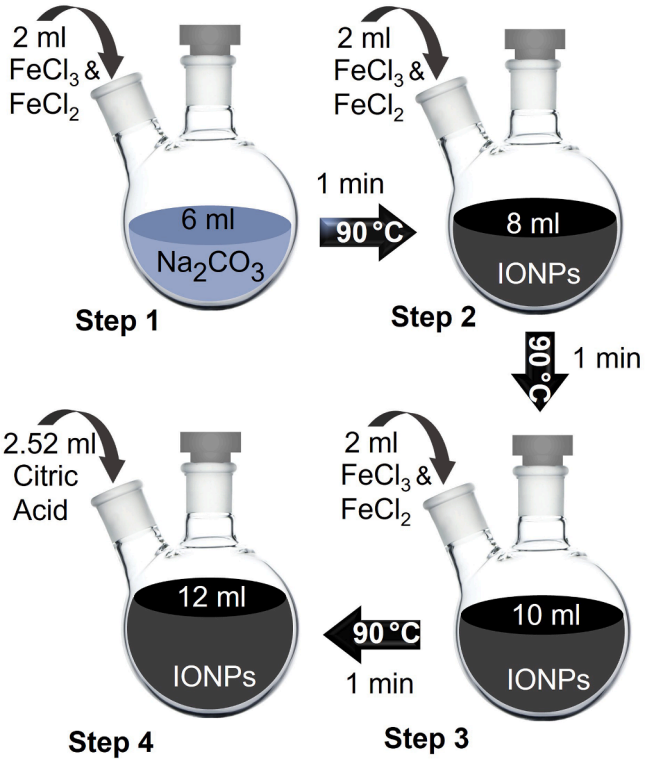

Fig. 1. Schematic of synthesis protocol for seeded growth batch synthesis of IONPs.

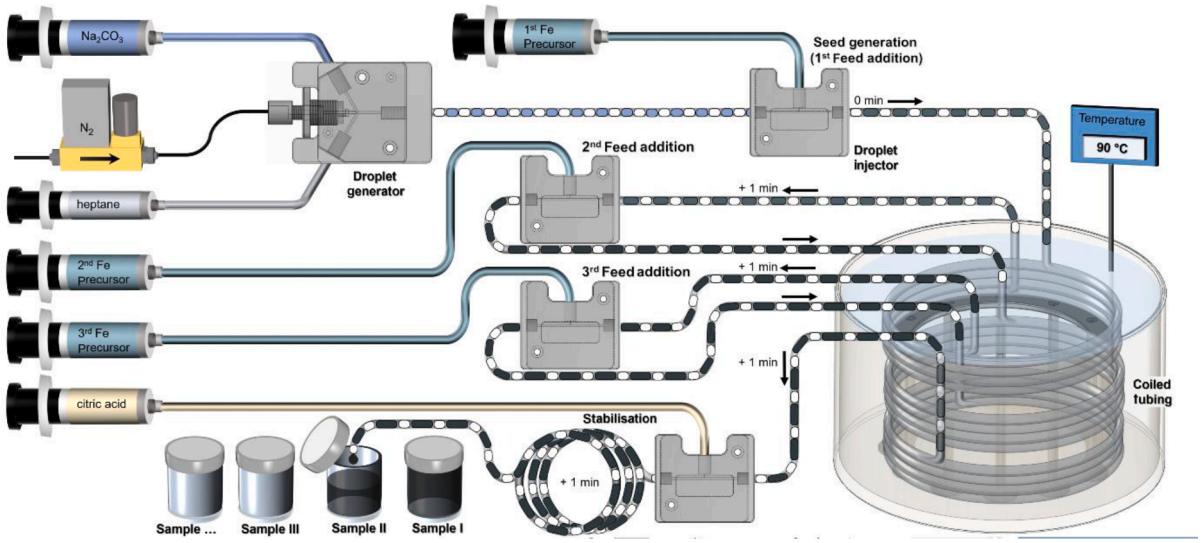

Fig. 2. Schematic of experimental setup for continuous IONP co-precipitation synthesis using a triphasic segmented flow reactor for seed generation, seeded grow via two additional feed addition steps, and stabilisation.

were used to connect the reactor components. Thus, the triphasic segmented flow reactor consisted of three main components, a) 1 droplet generator, where the triphasic segmented flow was formed, b) 4 T-junction droplet injectors, where the precursor solution or stabiliser solution was injected into the aqueous slugs (first three for Fe precursor solution addition and fourth for stabiliser solution addition), c) 1 straight tubing section to connect the droplet generator and the 1st T-junction droplet injector, 3 coiled tubing sections in a stainless steel coil holder to connect the subsequent T-junction droplet injectors, and 1 coiled tubing section to connect the final T-junction droplet injector and sampling vessel, providing residence time for the seed synthesis, the two growth steps and the stabilisation step. The length of the coils between the T-junction droplet injectors was varied to set the residence time desired for each step considering the total flow rate. The coils were submerged in a stirred water bath, with heat and magnetic stirring provided by a hotplate (C-MAG HS10, IKA) connected to a temperature controller (ETS-D5, IKA) for feedback control. For the video recordings at 240 fps of droplet formation and reagent solution addition into droplets, a back light with a suitable antiglare diffuser was used.

2.6. Self-seeded growth flow co-precipitation synthesis

Five syringe pumps (Harvard Apparatus, PHD Ultra) equipped with six 50 ml gas-tight syringes were used to individually control the reactant, stabiliser and carrier input streams into the flow reactor. Two syringes were placed in one syringe pump for the 2nd and 3rd Fe precursor solution additions. Nitrogen was fed to the droplet generator at atmospheric pressure via a mass flow controller (MFC, 0.1–5 ml/min EL-FLOW Prestige, Bronkhorst). Heptane was used as the carrier liquid and was fed at a low flow rate (0.2 ml/min), sufficient to isolate the droplets from the channel walls. To start up the reactor, heptane and nitrogen gas (0.4 ml/min) were introduced at the droplet generator to form gas–liquid two-phase flow. When the two-phase flow stabilised, and the reactor was filled, the base aqueous phase (Na_2CO_3 solution, 0.4 ml/min) was introduced at the droplet generator to form liquid–liquid-gas three-phase flow. After the three-phase flow stabilised, to start the flow synthesis the iron precursor solution was added at the 1st T-junction droplet injector followed by the 2nd and 3rd T-junction droplet injector and eventually citric acid solution at the 4th T-junction droplet injector. The temperature of the heating stages was increased to 90 °C, after stable three-phase segmentation was established throughout the reactor at room temperature. After reaching a stable flow regime and the desired reaction temperature, three times the total residence time of the reactor was allowed, for the reaction to reach a steady state before collecting samples. The samples were collected into vials, and the film of heptane at the top of IONP solution was removed by a pipette.

3. Results and discussion

3.1. IONPs via seeded growth batch co-precipitation

A seeded growth synthesis of IONPs via co-precipitation with one seed formation and two seeded growth steps followed by one stabilisation step was studied in batch experiments first, before designing a continuous flow process. For reduction of the iron precursors in the coprecipitation synthesis, a weak base, sodium carbonate was used, in contrast to widely reported sodium hydroxide [9], or ammonium hydroxide [53], as slow reaction rate favours seeded growth, while self-nucleation dominates at fast reaction rate [40].

Previous studies using the same iron precursors and base solutions showed that non-magnetic intermediate phases precipitate immediately after mixing the solutions. These intermediate phases then transition to magnetite in approximately 5–6 min at 60 °C [39]. So, for the initial batch experiments, the base and precursor solutions were added (separately, but at exactly the same time) in three steps at 60 °C, having 6 min reaction time between them. The nanoparticles synthesised with this protocol were 15 nm in core diameter, but comprised of intermediate phases along with magnetite (see Figure S1). Previous reports have shown that the magnetite formation step can be accelerated by increasing the reaction temperature to 90 °C [54]. Thus, the reaction temperature was increased to 90 °C which allowed to form magnetite for each step of seeded growth within < 1 min reaction time. This prevented the presence of intermediate phases at the shorter reaction time (see Figure S1) in comparison to 60 °C. This initial batch study showed that the seeded growth can increase the heating rate of the obtained IONPs significantly and ILP values of up to 1.63 nH m^2 kg_{Fe}^{-1} were achieved. However, the aforementioned batch synthesis protocol was difficult to translate into flow due to many reagent addition steps. To facilitate a transition into continuous flow synthesis, all of the base solution (Na_2CO_3) was added first in a single step, and Fe precursor solution was added in three steps instead of adding both reagents at every step (see Fig. 1). This did not reduce the magnetic heating ability and in fact yielded even higher magnetic heating power (ILP = 3.3 nH m^2 kg_{Fe}^{-1}). More information on particle size, XRD analysis and magnetic heating

performances of IONPs synthesised in batch experiments can be found in the supplementary information (section 2). With higher temperature preventing the presence of non-magnetite intermediate phases in the final product, faster reaction time and reduced number of addition steps, this optimised synthesis protocol was selected for batch to continuous flow translation.

After the growth steps, citric acid was added to enhance the colloidal stability of the nanoparticle suspension. Citric acid has been shown to be an effective stabiliser for co-precipitation synthesis even in the absence of any washing or ultrasonication step. It induces minor IONP dissolution yielding de-agglomeration, which makes stabilisation with carboxylic groups effective [29].

3.2. IONPs via co-precipitation in triphasic segmented flow reactor

3.2.1. Triphasic segmented flow reactor

Initially, single-phase flow experiments were performed in 1 mm I.D. FEP tubing in order to develop a continuous flow process for IONP synthesis following the batch chemistry discussed in section 3.1. The formation of particles was instantaneous when the base and precursor solutions came into contact, resulting in fouling and clogging of the flow reactor (see section 3 in supplementary information). To prevent the reaction mixture from coming in contact with the reactor walls, and for multipoint addition of precursors into the reacting phase, a triphasic segmented flow system (heptane-nitrogen-aqueous reaction mixture) was developed. Detailed description of the reactor is provided in the experimental section (2.5–2.6) and a schematic, image and videos of the whole reactor setup are presented in Fig. 2 and section 4 in supplementary information. At the droplet generator, three phases, organic liquid (heptane), gaseous (nitrogen), aqueous liquid (base) came in contact. After the release of each bubble, a triphasic segmented flow was formed (see video V2) in the hydrophobic outlet channel due to the different surface wettability of the continuous phase (heptane) and dispersed phase (aqueous base solution). In the T-junction droplet injectors, this uniform and controlled triphasic segmented flow enabled self-synchronised iron precursor injection only into the flowing dispersed phase aqueous droplets (see Figure S4 and video V3). Due to the hydrophobicity of the FEP block and subsequent FEP tubing walls, the aqueous precursor phase merged with the reacting phase droplets. This enabled the formation of IONPs synthesised within the reactive droplets enclosed by the continuous heptane phase without coming in contact with the reactor walls. The nitrogen gas bubbles functioned as spacers between two reacting droplets preventing droplet coalescence. IONPs formed rapidly once the precursor solution was injected into the droplets (initially carrying only the base solution) (see Figure S4). After the precursor addition, the uniform train of droplets with recirculating IONPs ensured uniform mixing. The formation of stable segmented flow was found to be essential for fouling-free operation and optimum performance of the synthesised particles. After formation of IONP seeds in the first feeding step of iron precursor, two subsequent feeding steps were used adding new iron precursor solution into the reacting droplets, enabling seeded growth. Finally, a fourth droplet injector was used for the addition of the citric acid stabiliser solution into the droplets with the already grown IONPs. Thus, the multistep addition batch synthesis was translated into multipoint addition continuous synthesis using a flow reactor, which can be operated for hours without any fouling.

3.2.2. Optimisation of flow parameters via DoE

A DoE study was performed seeking for the continuous flow conditions yielding the IONPs with optimum heating abilities for MHCT. Therefore, the effect of precursor flow rate and residence time of the seed generation and growth steps on the IONP's ILP and D_h was studied. The iron precursor solution flow rates, which were identical for seed generation, 2nd and 3rd feed addition step, were varied between 0.133 and 0.2 ml/min. The residence times for the seed synthesis and the two growth steps were varied between 1 and 2 min, by adapting the tube length between the T-junction droplet injectors (accounting for variations in the total flow rate). Precursor solution flow rates were not lower than 0.133 ml/min to avoid generation of non-magnetic phase impurities and were not higher than 0.2 ml/min to avoid isolated precursor droplets not mixing with the primary reacting droplet. A minimum residence time of 1 min was kept between T-junction droplet injectors, as it is the time required to form magnetite phases from the intermediate iron hydroxide carbonate phase [54]. Sodium carbonate solution, nitrogen, heptane and citric acid stabiliser solution flow rates were kept constant at 0.4, 0.4, 0.2 and 0.168 ml/min respectively. The temperature was not varied as traces of non-magnetite phases were observed when the reaction temperature was < 90 °C. A DoE matrix was constructed using three-level two-factor custom design to reduce the experimental effort and to design a plan to guide the experiments. The DoE matrix with all 12 experimental conditions and the responses (ILP and D_h) is summarised in the supplementary information (Table S4). The flexibility of the reactor platform allowed to conveniently screen the iron precursor flow rates for each of the tubing lengths (giving the different residence times) tested. This prevented any operator effect when performing the experiments, unlike typical screening of synthetic conditions via batch procedures. Responses generated by the flow experiments were used to build a response surface model (RSM) to predict ILP and D_h. Fig. 3 shows the response surfaces (ILP and D_h) for varying residence times and iron precursor flow rates for the seed synthesis and the two growth steps.

Successful prediction of the ILP and particle size within a 95% confidence interval was possible with a quadratic fit using a two-parameter continuous RSM (see Figure S5). Assessing the goodness of fit via the analysis of variance test for the models, the R^2 was equal to 0.98 and 0.97 for ILP and D_h, respectively indicating the accuracy of the developed RSM. The RSM prediction expressions (equation ES1 and equation ES2 in the supplementary information) show the strong interaction between the two parameters. These equations can be used to tune the ILP and D_h within the studied range of residence times and Fe precursor solution flow rates. Due to this non-linearity between the process parameters screened and ILP and D_h, it was important to validate the RSM. Validation experiments performed at parameter values not used to train the RSM showed good agreement between predicted and experimentally observed ILP and D_h (see Figure S6a-b).

All conditions yielded colloidally stable IONPs, but high heating performances were observed around the 1 min residence time and 1.33 ml/min precursor solution flow rate. At higher Fe precursor solution flow rate, hence higher Fe concentration, the D_h was observed to decrease, which correlates with a reduced heating ability (see Fig. 3a-3b). D_h in the range of 70–90 nm was observed to yield the best heating particles. Longer residence times resulted in further growth (indicated by increased D_{TEM}) and aggregation (indicated by increased D_h) of the IONPs, which adversely impacted the IONPs' heating performance (see Fig. 3). This was attributed to demagnetising interactions between the cores, as the number of cores in these aggregated multi-core particles increased [29]. Fig. 4 shows representative TEM images of the IONPs synthesised at the longest residence time (2 min) and at the highest Fe precursor solution flow rate (0.2 ml/min). The highest ILP of the IONPs was obtained at 0.133 ml/min Fe precursor solution flow rate and 1 min residence time for each step (No. 4 in Table S4). A detailed study of the flow synthesis at these conditions is shown in the next section.

3.2.3. Three-step seeded growth synthesis of IONPs at optimised conditions

The synthetic conditions which yielded IONPs with the optimum heating ability (No. 4 in Table S4) were studied in detail. TEM images

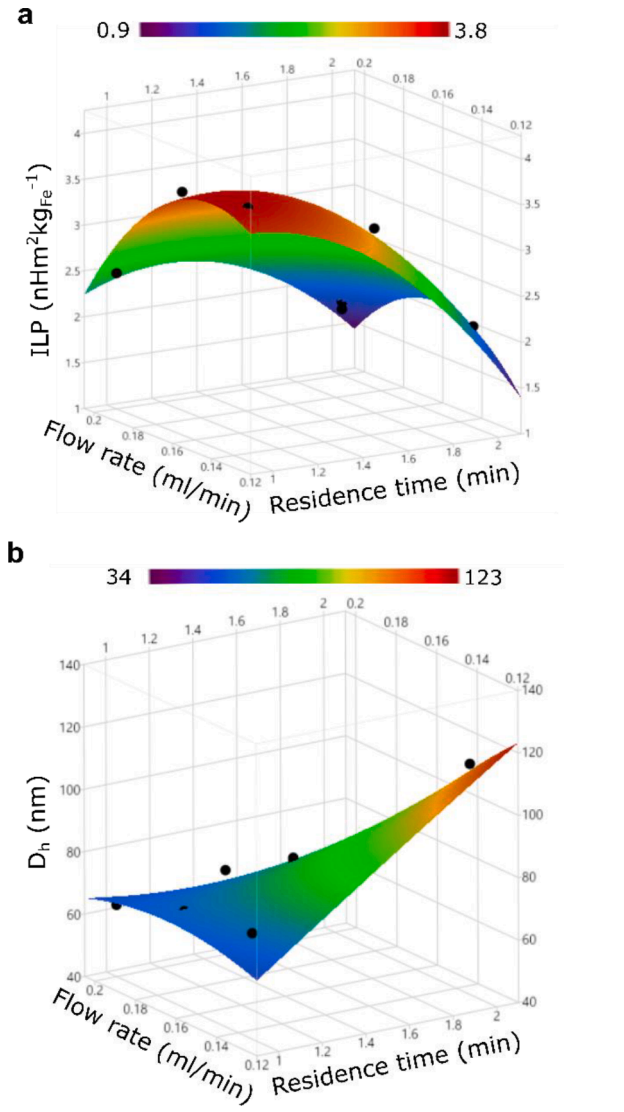

Fig. 3. Response surface plots showing the effect of the iron precursor solution flow rate and residence time, (equal for the seed synthesis and the two seeded growth steps) on (a) the intrinsic loss power, ILP, and (b) the hydrodynamic diameter, D_h. The black points are the experimental data.

of citric acid stabilised IONPs showed a multi-core structure, consisting of spheroidal nanocrystallite building blocks. TEM analysis (Fig. 5a) showed an increase in IONP core size (D_{TEM}) with each growth step, i.e., from $D_{TEM} = 12.0 \pm 2.5$ nm (IONP seeds, 1st feed addition) to $D_{TEM} = 13.2 \pm 3.4$ nm after the 1st growth step (2nd feed addition), and to $D_{TEM} = 15.3 \pm 3.3$ nm after the 2nd growth step (3rd feed addition). The IONP size distribution from the corresponding TEM images is shown in Fig. 5a. The average crystallite size (D_{XRD}) obtained from XRD analysis also increased from $D_{XRD} = 12.8$ nm (IONP seeds) to $D_{XRD} = 13.8$ nm after the 1st growth step and to $D_{XRD} = 15.8$ nm after the 2nd growth step. This is consistent with the results obtained from the TEM analysis (compared in Fig. 5b). DLS analysis showed an increase in the IONPs' D_h with each precursor feeding step, i.e., increasing from $D_h = 48$ nm (IONP seeds) to $D_h = 69$ nm and to $D_h = 74$ nm in 1st and 2nd growth steps respectively. The higher D_h than the core size of the NPs (D_{TEM}) confirms the clustered multi-core structure of the colloidally stable IONPs. This shows that both the size of clustered IONPs as well as single-core crystalline building blocks grow with each feed addition step. The simultaneous increase of IONP cluster size/nanocrystallite size and D_h correlated with better magnetic

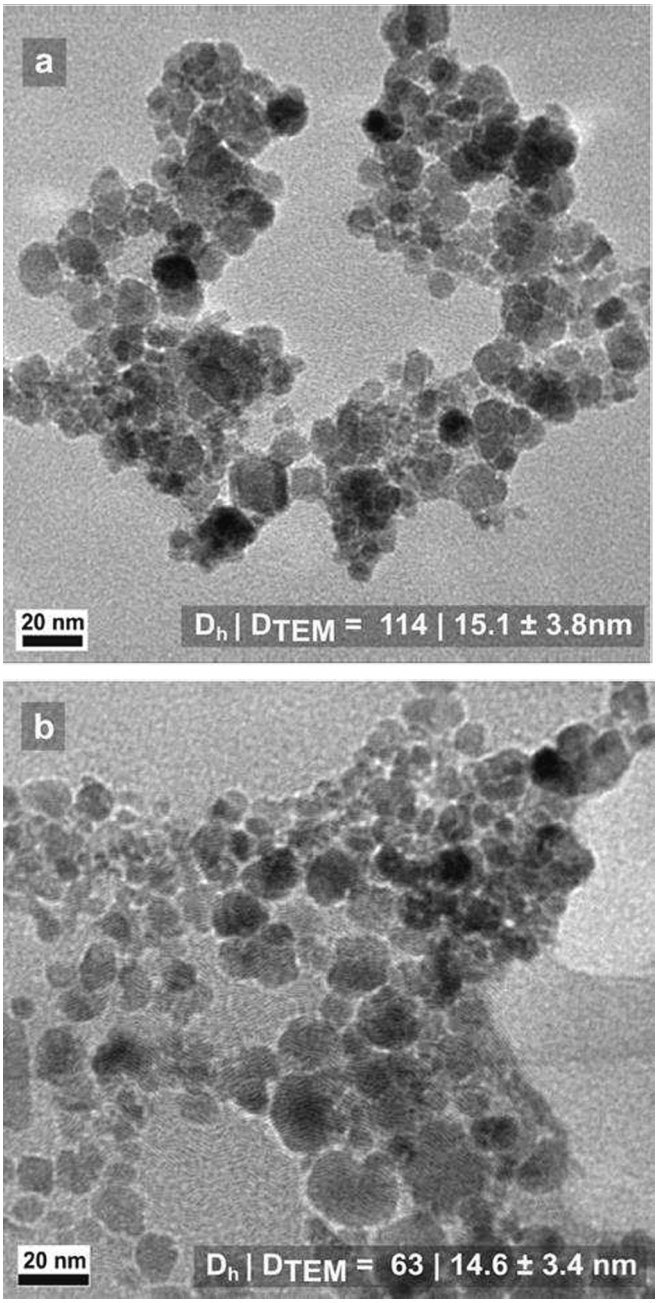

Fig. 4. Representative TEM images of IONPs synthesised in the triphasic flow reactor at (a) 2 min residence time of each step and 0.133 ml/min Fe precursor solution flow rate (No. 3 in Table S4); (b) 1 min residence time of each step and 0.2 ml/min Fe precursor solution flow rate (No. 5 in Table S4) in each step.

heating performance, i.e., higher ILP values. Fig. 5b shows that the ILP of the IONPs increased with particle size. Fig. 5c demonstrates the improved heating performance of the seeded-grown IONPs, with ILP values increasing with each growth step.

It is important to highlight that the size increase of the individual IONP cores is known to enhance heating rates only when they exceed 10 nm [24,25,27,55]. Also, the formation of clusters can improve the heating ability of the IONPs [28]. However, bigger individual cores are essential, as clustering of IONPs smaller than 10 nm will not yield good heaters. The size increase of the individual cores as well as clustering are both responsible for the good magnetic heating performance.

The $D_{TEM} = 15.3$ nm IONPs synthesised with the seeded growth process exhibited excellent heating performance with ILP value 3.76 nH m^2 kg_{Fe}^{-1}, exceeding those of commercially available IONPs (ILP up to 3

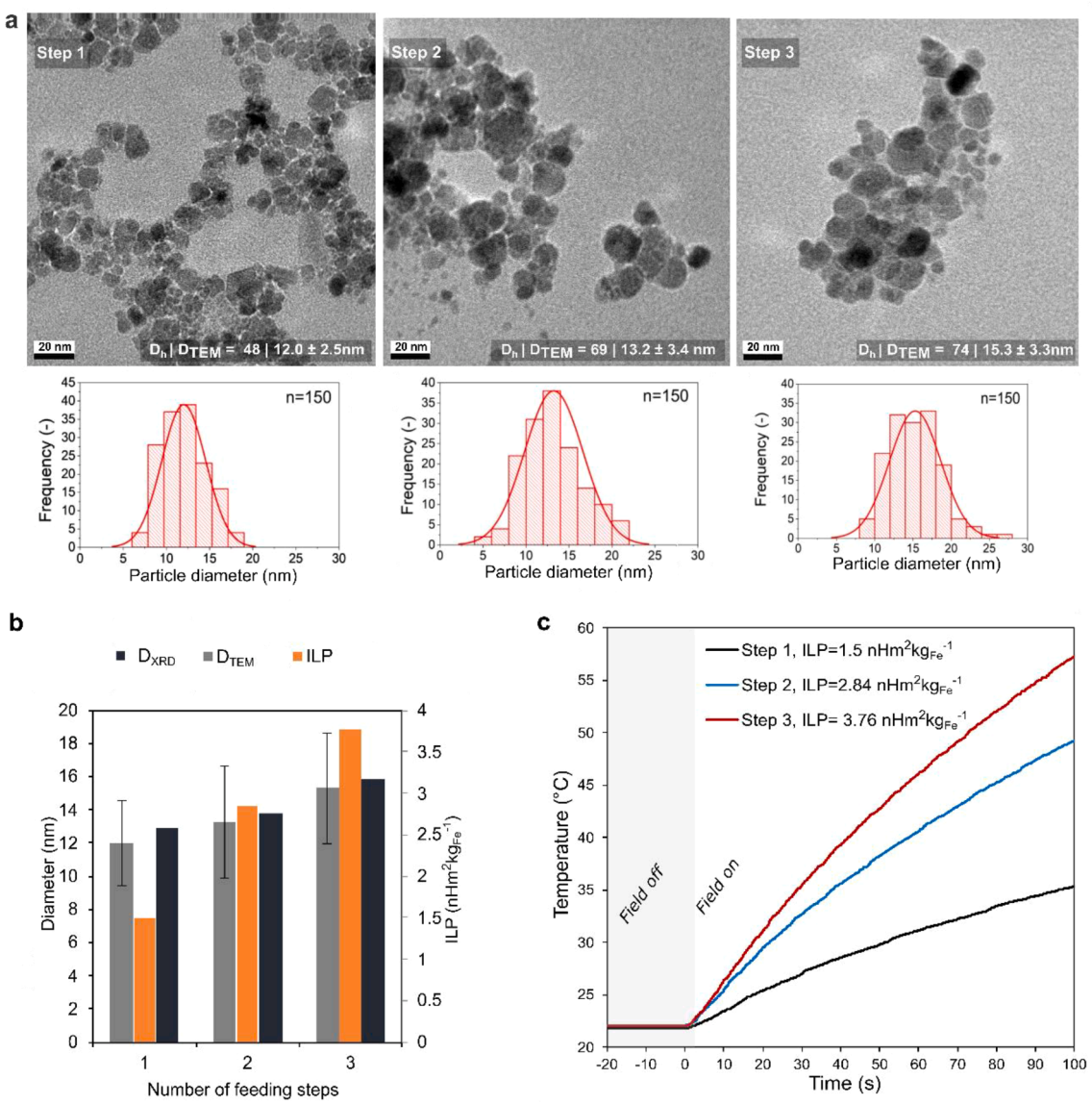

Fig. 5. (a) Representative TEM images with particle size distribution of IONPs obtained at 1 min residence time of each step and 0.133 ml/min Fe precursor solution flow rate in each step (No. 4 in Table S4). (b) Variation in D_{TEM}, D_{XRD} and ILP with the number of Fe precursor feeding steps. (c) Heating profiles of IONPs grown with different number of feeding steps at a magnetic field strength of 308 G and a frequency of 488 kHz.

nH m^2 kg_{Fe}^{-1}) [56–58]. The heating performance and D_h of the optimised IONPs was stable over the monitored time span of several months (see Figure S7), demonstrating their excellent colloidal stability. The yield of IONPs based on fed iron precursors was found to be 79.7, 80.2 and 81.4 % after seed formation, 1st and 2nd growth steps respectively.

The diffractograms of IONPs obtained using different number of feeding steps are shown in Fig. 6a. The XRD patterns show that even after the 1st Fe precursor feeding step, magnetite was the only evident crystalline phase and there was no sign of any crystalline intermediate phases.

Fig. 6b shows the magnetisation curves of dried IONPs synthesised with the three-step seeded growth process. At 300 K the magnetisation curve was anhysteretic, i.e., it was linear and crossed the origin, indicating negligible coercivity and superparamagnetic behavior of the IONPs at room temperature. The saturation mass magnetisation at 300 K was measured to be 102.4 emu/g_{Fe}.

These saturation magnetisation values are below the bulk magnetisation (103 and 128 emu/g_{Fe} for maghemite and magnetite) [59], as surface effects cause a substantial reduction in the magnetisation. The zero-field cooling and field cooling curves, show that the blocking temperature was 305 K. This too shows that IONPs are superparamagnetic at room temperature (see Figure S8), but indicates that a further increase in particle size (either due to larger core or cluster sizes) is likely to exceed the superparamagnetic limit, i.e., agglomerates are more likely to form due to magnetic attraction between particles [18,60].

4. Conclusion

We demonstrated a triphasic (liquid–liquid-gas) segmented flow reactor platform showcasing the potential to perform complex fouling-prone multistep synthesis of nanomaterials via flexible multipoint addition of reagents. Due to the modular nature of the reactor platform, there is flexibility to tune the droplet sizes, to have multiple numbers of reagent addition steps, and to use temperature-controlled residence time modules between reagent addition steps. Four reagent addition steps by means of custom-designed T-junction droplet injectors were successfully performed. The analysis and design principles presented in this work are general. This modular reactor platform can be extended to other complex multistep nanomaterial synthesis chemistries in continuous flow,

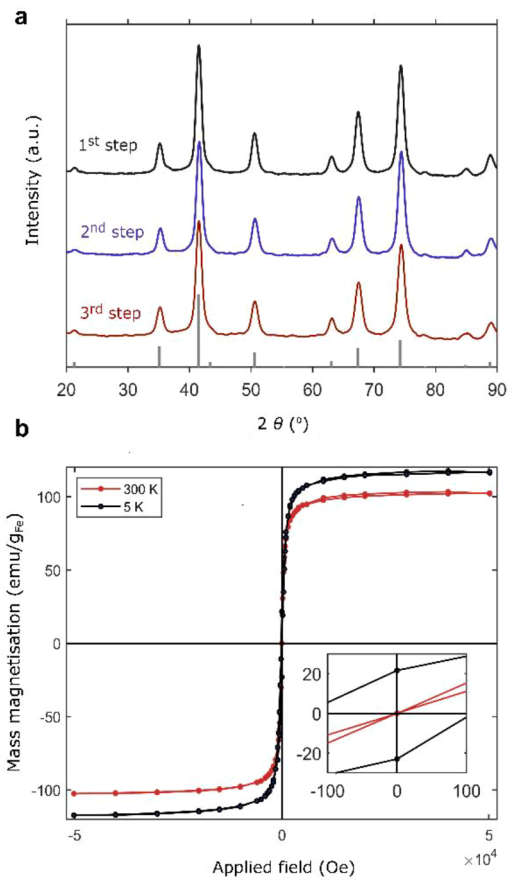

Fig. 6. (a) XRD patterns of IONPs synthesised with different number of Fe precursor feeding steps. The bars at the bottom show the peak positions and relative intensities corresponding to magnetite (PDF ref. 03–065-3107); (b) Magnetic hysteresis curves of IONPs synthesised with three Fe precursor feeding steps.

where multiple additions of the reagents are essential. The droplet generator and droplet injector blocks can be submerged in a temperature bath for chemistries requiring high temperatures. For such chemistries, a pressurised system can be used with a backpressure regulator to prevent the increased gas volumes, resulting in jetting of droplets inside the coil. The triphasic segmented flow reactor platform was demonstrated for a batch to flow translation of synthesising citric acid stabilised magnetic IONPs via a three-step self-seeded growth synthesis. The process, which involves initial synthesis of IONP seeds followed by their two-step gradual growth with further precursor addition and finally stabilisation by citric acid addition, was run for 2 h without any sign of reactor fouling. The aqueous co-precipitation synthetic method produced colloidally stable magnetic nanoparticles with good heating performance (ILP up to 3.76 nH m^2 kg_{Fe}^{-1}) in alternating magnetic fields, which is important for magnetic hyperthermia cancer treatment. A DoE study enabled a systematic exploration of the design space to optimise IONP heating performance. A response surface model was developed to tune and predict nanoparticle hydrodynamic diameter and magnetic heating performance based on residence time of each step and iron precursor flow rate in each step as controlling parameters and showed good accuracy. The green and cost-effective (<5 £/g_{IONP}) synthesis of colloidally stable IONPs was achieved without any additives, avoiding expensive or toxic chemicals and high temperatures compared to widely used organic synthesis counterparts for magnetic hyperthermia. The clogging and fouling-free nature of the reactor platform, along with the flexibility to perform complex multistep chemistries at high temperature can open the path for rapid screening of synthetic conditions for complex multistep chemistries.

Declaration of Competing Interest

The authors declare that they have no known competing financial interests or personal relationships that could have appeared to influence the work reported in this paper.

Data availability

Data will be made available on request.

Acknowledgements

The authors would like to thank the EPSRC UK for financial support (EP/M015157/1) through the Manufacturing Advanced Functional Materials (MAFuMa) scheme.

Appendix A. Supplementary data

Supplementary data to this article can be found online at https://doi.org/10.1016/j.cej.2023.142007.

References

[1] V. Sebastian, S.A. Khan, A.A. Kulkarni, Perspective article: flow synthesis of functional materials, J. Flow Chem. 7 (2017) 96–105, https://doi.org/10.1556/1846.2017.00028.
[2] J. Park, A. Saffari, S. Kumar, A. Günther, E. Kumacheva, Microfluidic synthesis of polymer and inorganic particulate materials, Annu. Rev. Mat. Res. 40 (2010) 415–443, https://doi.org/10.1146/ANNUREV-MATSCI-070909-104514.
[3] H. Huang, H. du Toit, L. Panariello, L. Mazzei, A. Gavriilidis, Continuous synthesis of gold nanoparticles in micro and millifluidic systems, Physical Sciences Reviews 6 (2021), https://doi.org/10.1515/psr-2017-0119.
[4] R.L. Hartman, Managing solids in microreactors for the upstream continuous processing of fine chemicals, Org. Process Res. Dev. 16 (2012) 870–887, https://doi.org/10.1021/OP200348T.
[5] S. Pal, A.A. Kulkarni, Interfacial precipitation and clogging in straight capillaries, Chem. Eng. Sci. 153 (2016) 344–353, https://doi.org/10.1016/j.ces.2016.07.012.
[6] A.A. Lapkin, K. Loponov, G. Tomaiuolo, S. Guido, Solids in continuous flow reactors for specialty and pharmaceutical syntheses. First edition. Edited by Luigi Vaccaro, Sustainable flow chemistry: Methods and applications (2017) 277–308, 10.1002/9783527689118.CH11.
[7] S. Pal, A.A. Kulkarni, Quantitative comparison of strategies to delay clogging in straight capillaries, Chem. Eng. Sci. 199 (2019) 88–99, https://doi.org/10.1016/J.CES.2019.01.015.
[8] S. Sebastián, N. Zaborenko, L. Gu, K.F. Jensen, Microfluidic assisted synthesis of hybrid Au−Pd dumbbell-like nanostructures: sequential addition of reagents and ultrasonic radiation, Cryst. Growth Des. 17 (2017) 2700–2710, https://doi.org/10.1021/acs.cgd.7b00193.
[9] M.O. Besenhard, A.P. LaGrow, A. Hodzic, M. Kriechbaum, L. Panariello, G. Bais, K. Loizou, S. Damilos, M. Margarida Cruz, N.T.K. Thanh, A. Gavriilidis, Co-precipitation synthesis of stable iron oxide nanoparticles with NaOH: new insights and continuous production via flow chemistry, Chemical Engineering Journal 399 (2020) 125740, 10.1016/j.cej.2020.
[10] M. Schoenitz, L. Grundemann, W. Augustin, S. Scholl, Fouling in microstructured devices: a review, Chem. Commun. 51 (2015) 8213–8228, https://doi.org/10.1039/C4CC07849G.
[11] K. Kumar, A.M. Nightingale, S.H. Krishnadasan, N. Kamaly, M. Wylenzinska-Arridge, K. Zeissler, W.R. Branford, E. Ware, A.J. de Mello, J.C. de Mello, Direct synthesis of dextran -coated superparamagnetic iron oxide nanoparticles in a capillary-based droplet reactor, J. Mater. Chem. 22 (2012) 4704–4708, https://doi.org/10.1039/C2JM30257H.
[12] J.M. Köhler, S. Li, A. Knauer, Why is micro segmented flow particularly promising for the synthesis of nanomaterials ? Chem. Eng. Technol. 36 (2013) 887–899, https://doi.org/10.1002/CEAT.201200695.
[13] L. Panariello, L. Mazzei, A. Gavriilidis, Modelling the synthesis of nanoparticles in continuous microreactors: the role of diffusion and residence time distribution on nanoparticle characteristics, Chem. Eng. J. 350 (2018) 1144–1154, https://doi.org/10.1016/J.CEJ.2018.03.167.
[14] I. Lignos, Y. Mo, L. Carayannopoulos, M. Ginterseder, M.G. Bawendi, K.F. Jensen, A high-temperature continuous stirred-tank reactor cascade for the multistep synthesis of InP/ZnS quantum dots, React, Chem. Eng. 6 (2021) 459–464, https://doi.org/10.1039/D0RE00454E.
[15] K. Tacsi, Á. Joó, É. Pusztai, A. Domokos, Z.K. Nagy, G. Marosi, H. Pataki, Development of a triple impinging jet mixer for continuous antisolvent crystallization of acetylsalicylic acid reaction mixture, Chem. Eng. Process. 165 (2021), 108446, https://doi.org/10.1016/J.CEP.2021.108446.
[16] R. Baber, L. Mazzei, N.T.K. Thanh, A. Gavriilidis, Synthesis of silver nanoparticles using a microfluidic impinging jet reactor, J. Flow. Chem. 6 (2016) 268–278, https://doi.org/10.1556/1846.2016.00015.

[17] F. Assa, H. Jafarizadeh-Malmiri, H. Ajamein, N. Anarjan, H. Vaghari, Z. Sayyar, A. Berenjian, A biotechnological perspective on the application of iron oxide nanoparticles, Nano Res. 9 (2016) 2203–2225, https://doi.org/10.1007/s12274-016-1131-9.

[18] S. Gul, S.B. Khan, I.U. Rehman, M.A. Khan, M.I. Khan, A comprehensive review of magnetic nanomaterials modern day theranostics, Front. Mater. 6 (2019) 179, https://doi.org/10.3389/fmats.2019.00179.

[19] Q. Feng, Y. Liu, J. Huang, K. Chen, J. Huang, K. Xiao, Uptake, distribution, clearance, and toxicity of iron oxide nanoparticles with different sizes and coatings, Sci. Rep. 8 (2018) 1–13, https://doi.org/10.1038/s41598-018-19628-z.

[20] F. Soetaert, P. Korangath, D. Serantes, S. Fiering, R. Ivkov, Cancer therapy with iron oxide nanoparticles: Agents of thermal and immune therapies, Adv. Drug Deliv. Rev. 163–164 (2020) 65–83, https://doi.org/10.1016/J.ADDR.2020.06.025.

[21] C. Blanco-Andujar, A. Walter, G. Cotin, C. Bordeianu, D. Mertz, D. Felder-Flesch, S. Begin-Colin, Design of iron oxide-based nanoparticles for MRI and magnetic hyperthermia, Nanomedicine 11 (2016) 1889–1910, https://doi.org/10.2217/nnm-2016-5001.

[22] I. Rubia-Rodríguez, A. Santana-Otero, S. Spassov, E. Tombácz, C. Johansson, P. de La Presa, F.J. Teran, M.D.P. Morales, S. Veintemillas-Verdaguer, N.T.K. Thanh, M. O. Besenhard, C. Wilhelm, F. Gazeau, Q. Harmer, E. Mayes, B.B. Manshian, S. J. Soenen, Y. Gu, Á. Millán, E.K. Efthimiadou, J. Gaudet, P. Goodwill, J. Mansfield, U. Steinhoff, J. Wells, F. Wiekhorst, D. Ortega, Whither magnetic hyperthermia? a tentative roadmap, Materials 14 (2021) 706, https://doi.org/10.3390/MA14040706.

[23] M. Levy, A. Quarta, A. Espinosa, A. Figuerola, C. Wilhelm, M. García-Hernández, A. Genovese, A. Falqui, D. Alloyeau, R. Buonsanti, P.D. Cozzoli, M.A. García, F. Gazeau, T. Pellegrino, Correlating magneto-structural properties to hyperthermia performance of highly monodisperse iron oxide nanoparticles prepared by a seeded-growth route, Chem. Mater. 23 (2011) 4170–4180, https://doi.org/10.1021/cm201078f.

[24] J.P. Fortin, C. Wilhelm, J. Servais, C. Ménager, J.C. Bacri, F. Gazeau, Size-sorted anionic iron oxide nanomagnets as colloidal mediators for magnetic hyperthermia, J. Am. Chem. Soc. 129 (2007) 2628–2635, https://doi.org/10.1021/JA067457E.

[25] S. Tong, C.A. Quinto, L. Zhang, P. Mohindra, G. Bao, Size-dependent heating of magnetic iron oxide nanoparticles, ACS Nano 11 (2017) 6808–6816, https://doi.org/10.1021/acsnano.7b01762.

[26] M. Gonzales-Weimuller, M. Zeisberger, K.M. Krishnan, Size-dependant heating rates of iron oxide nanoparticles for magnetic fluid hyperthermia, J. Magn. Magn. Mater. 321 (2009) 1947–1950, https://doi.org/10.1016/J.JMMM.2008.12.017.

[27] P. de La Presa, Y. Luengo, M. Multigner, R. Costo, M.P. Morales, G. Rivero, A. Hernando, Study of heating efficiency as a function of concentration, size, and applied field in γ-Fe_2O_3 nanoparticles, J. Phys. Chem. C 116 (2012) 25602–25610, https://doi.org/10.1021/jp310771p.

[28] L. Storozhuk, M.O. Besenhard, S. Mourdikoudis, A.P. LaGrow, M.R. Lees, L. D. Tung, A. Gavriilidis, N.T.K. Thanh, Stable iron oxide nanoflowers with exceptional magnetic heating efficiency: simple and fast polyol synthesis, ACS Appl. Mater. Interfaces 13 (2021) 45870–45880, https://doi.org/10.1021/ACSAMI.1C12323.

[29] C. Blanco-Andujar, D. Ortega, P. Southern, Q.A. Pankhurst, N.T.K. Thanh, High performance multi-core iron oxide nanoparticles for magnetic hyperthermia: microwave synthesis, and the role of core-to-core interactions, Nanoscale 7 (2015) 1768–1775, https://doi.org/10.1039/C4NR06239F.

[30] Z. Shaterabadi, G. Nabiyouni, M. Soleymani, Correlation between effects of the particle size and magnetic field strength on the magnetic hyperthermia efficiency of dextran-coated magnetite nanoparticles, Mater. Sci. Eng. C 117 (2020), 111274, https://doi.org/10.1016/J.MSEC.2020.111274.

[31] P.J. Sugumaran, X.L. Liu, T.S. Herng, E. Peng, J. Ding, GO-functionalized large magnetic iron oxide nanoparticles with enhanced colloidal stability and hyperthermia performance, ACS Appl. Mater. Interfaces 11 (2019) 22703–22713, https://doi.org/10.1021/acsami.9b04261.

[32] R. Massart, Preparation of aqueous magnetic liquids in alkaline and acidic media, IEEE Trans. Magn. 17 (1981) 1247–1248, https://doi.org/10.1109/TMAG.1981.1061188.

[33] A.A. Olowe, J.M.R. Génin, The mechanism of oxidation of ferrous hydroxide in sulphated aqueous media: importance of the initial ratio of the reactants, Corros. Sci. 32 (1991) 965–984, https://doi.org/10.1016/0010-938x(91)90016-i.

[34] T. Asimakidou, A. Makridis, S. Veintemillas-Verdaguer, M.P. Morales, I. Kellartzis, M. Mitrakas, G. Vourlias, M. Angelakeris, K. Simeonidis, Continuous production of magnetic iron oxide nanocrystals by oxidative precipitation, Chem. Eng. J. 393 (2020), 124593, https://doi.org/10.1016/J.CEJ.2020.124593.

[35] D.A. Patiño-Ruiz, S.I. Meramo-Hurtado, Á.D. González-Delgado, A. Herrera, Environmental sustainability evaluation of iron oxide nanoparticles synthesized via green synthesis and the coprecipitation method: a comparative life cycle assessment study, ACS Omega 6 (2021) 12410–12423, https://doi.org/10.1021/acsomega.0c05246.

[36] L.A. Thomas, L. Dekker, M. Kallumadil, P. Southern, M. Wilson, S.P. Nair, Q. A. Pankhurst, I.P. Parkin, Carboxylic acid -stabilised iron oxide nanoparticles for use in magnetic hyperthermia, J. Mater. Chem. 19 (2009) 6529–6535, https://doi.org/10.1039/B908187A.

[37] A.R. Yasemian, M. Almasi Kashi, A. Ramazani, Surfactant-free synthesis and magnetic hyperthermia investigation of iron oxide (Fe_3O_4) nanoparticles at different reaction temperatures, Mater. Chem. Phys. 230 (2019) 9–16, https://doi.org/10.1016/j.matchemphys.2019.03.032.

[38] V. Narayanaswamy, S. Sambasivam, A. Saj, S. Alaabed, B. Issa, I.A. Al-Omari, I. M. Obaidat, Role of magnetite nanoparticles size and concentration on hyperthermia under various field frequencies and strengths, Molecules 26 (2021) 796, https://doi.org/10.3390/molecules26040796.

[39] A.P. Lagrow, M.O. Besenhard, A. Hodzic, A. Sergides, L.K. Bogart, A. Gavriilidis, N. T.K. Thanh, Unravelling the growth mechanism of the co-precipitation of iron oxide nanoparticles with the aid of synchrotron X-Ray diffraction in solution, Nanoscale 11 (2019) 6620–6628, https://doi.org/10.1039/C9NR00531E.

[40] C. Gao, J. Goebl, Y. Yin, Seeded growth route to noble metal nanostructures, J. Mater. Chem. C 1 (2013) 3898–3909, https://doi.org/10.1039/C3TC30365A.

[41] J.H. Huang, H.J. Parab, R.S. Liu, T.C. Lai, M. Hsiao, C.H. Chen, H.S. Sheu, J. M. Chen, D.P. Tsai, Y.K. Hwu, Investigation of the growth mechanism of iron oxide nanoparticles via a seed-mediated method and its cytotoxicity studies, J. Phys. Chem. C 112 (2008) 15684–15690, https://doi.org/10.1021/JP803452J.

[42] A. Espinosa, A. Muñoz-Noval, M. García-Hernández, A. Serrano, J. Jiménez De La Morena, A. Figuerola, A. Quarta, T. Pellegrino, C. Wilhelm, M.A. García, Magnetic properties of iron oxide nanoparticles prepared by seeded-growth route, J. Nanopart. Res. 15 (2013) 1–13, https://doi.org/10.1007/s11051-013-1514-8.

[43] A.M. Nightingale, T.W. Phillips, J.H. Bannock, J.C. de Mello, Controlled multistep synthesis in a three-phase droplet reactor, Nature, Communications 5 (2014) 1–8, https://doi.org/10.1038/ncomms4777.

[44] S. Duraiswamy, S.A. Khan, Dual-stage continuous-flow seedless microfluidic synthesis of anisotropic gold nanocrystals, Part. Part. Syst. Char. 31 (2014) 429–432, https://doi.org/10.1002/PPSC.201300266.

[45] W.K. Wong, S.K. Yap, Y.C. Lim, S.A. Khan, F. Pelletier, E.C. Corbos, Robust, non-fouling liters-per-day flow synthesis of ultra-small catalytically active metal nanoparticles in a single-channel reactor, React, Chem. Eng. 2 (2017) 636–641, https://doi.org/10.1039/C7RE00072C.

[46] K. Abdel-Latif, R.W. Epps, F. Bateni, S. Han, K.G. Reyes, M. Abolhasani, K. Abdel-Latif, R.W. Epps, F. Bateni, S. Han, M. Abolhasani, K.G. Reyes, Self-driven multistep quantum dot synthesis enabled by autonomous robotic experimentation in flow, Advanced Intelligent Systems. 3 (2021) 2000245, https://doi.org/10.1002/aisy.202000245.

[47] D. Karan, S.A. Khan, Mesoscale triphasic flow reactors for metal catalyzed gas–liquid reactions, React. Chem. Eng. 4 (2019) 1331–1340, https://doi.org/10.1039/C9RE00150F.

[48] M.O. Besenhard, S. Pal, L. Storozhuk, S. Dawes, N.T.K. Thanh, L. Norfolk, S. Staniland, A. Gavriilidis, A versatile non-fouling multi-step flow reactor platform: demonstration for partial oxidation synthesis of iron oxide nanoparticles, Lab Chip 23 (2023) 115–124, https://doi.org/10.1039/D2LC00892K.

[49] M.C. Mascolo, Y. Pei, T.A. Ring, Room temperature co-precipitation synthesis of magnetite nanoparticles in a large pH window with different bases, Materials 6 (2013) 5549–5567, https://doi.org/10.3390/ma6125549.

[50] R.R. Wildeboer, P. Southern, Q.A. Pankhurst, On the reliable measurement of specific absorption rates and intrinsic loss parameters in magnetic hyperthermia materials, J. Phys. D Appl. Phys. 47 (2014), 495003, https://doi.org/10.1088/0022-3727/47/49/495003.

[51] K. Loizou, S. Mourdikoudis, A. Sergides, M.O. Besenhard, C. Sarafidis, K. Higashimine, O. Kalogirou, S. Maenosono, N.T.K. Thanh, A. Gavriilidis, Rapid millifluidic synthesis of stable high magnetic moment FexCy nanoparticles for hyperthermia, ACS Appl. Mater. Interfaces 12 (2020) 28520–28531, https://doi.org/10.1021/acsami.0c06192.

[52] M.O. Besenhard, L. Panariello, C. Kiefer, A.P. Lagrow, L. Storozhuk, F. Perton, S. Begin, D. Mertz, N.T.K. Thanh, A. Gavriilidis, Small iron oxide nanoparticles as MRI T1 contrast agent: scalable inexpensive water-based synthesis using a flow reactor, Nanoscale 13 (2021) 8795–8805, https://doi.org/10.1039/d1nr00877c.

[53] I.S. Smolkova, N.E. Kazantseva, V. Babayan, J. Vilcakova, N. Pizurova, P. Saha, The role of diffusion-controlled growth in the formation of uniform iron oxide nanoparticles with a link to magnetic hyperthermia, Cryst. Growth Des. 17 (2017) 2323–2332, https://doi.org/10.1021/acs.cgd.6b01104.

[54] M.O. Besenhard, D. Jiang, Q.A. Pankhurst, P. Southern, S. Damilos, L. Storozhuk, A. Demosthenous, N.T.K. Thanh, P. Dobson, A. Gavriilidis, Development of an in-line magnetometer for flow chemistry and its demonstration for magnetic nanoparticle synthesis, Lab Chip 21 (2021) 3775–3783, https://doi.org/10.1039/D1LC00425E.

[55] L. Lartigue, C. Innocenti, T. Kalaivani, A. Awwad, M.D.M. Sanchez Duque, Y. Guari, J. Larionova, C. Gueírin, J.L.G. Montero, V. Barragan-Montero, P. Arosio, A. Lascialfari, D. Gatteschi, C. Sangregorio, Water-dispersible sugar-coated iron oxide nanoparticles. An evaluation of their relaxometric and magnetic hyperthermia properties, J. Am. Chem. Soc. 133 (2011) 10459–10472, https://doi.org/10.1021/JA111448T.

[56] O.L. Lanier, O.I. Korotych, A.G. Monsalve, D. Wable, S. Savliwala, N.W.F. Grooms, C. Nacea, O.R. Tuitt, J. Dobson, Evaluation of magnetic nanoparticles for magnetic fluid hyperthermia, Int. J. Hyperth. 36 (2019) 687–701, https://doi.org/10.1080/02656736.2019.1628313.

[57] M. Kallumadil, M. Tada, T. Nakagawa, M. Abe, P. Southern, Q.A. Pankhurst, Suitability of commercial colloids for magnetic hyperthermia, J. Magn. Magn. Mater. 321 (2009) 1509–1513, https://doi.org/10.1016/J.JMMM.2009.02.075.

[58] D. Sakellari, S. Mathioudaki, Z. Kalpaxidou, K. Simeonidis, M. Angelakeris, Exploring multifunctional potential of commercial ferrofluids by magnetic particle hyperthermia, J. Magn. Magn. Mater. 380 (2015) 360–364, https://doi.org/10.1016/J.JMMM.2014.10.042.

[59] D. Dunlop, Ö. Özdemir, Rock magnetism: fundamentals and frontiers, Cambridge University Press, Cambridge, 1997.

[60] D. Ho, X. Sun, S. Sun, Monodisperse magnetic nanoparticles for theranostic applications, Acc. Chem. Res. 44 (2011) 875–882, https://doi.org/10.1021/ar200090c.